Resonance Raman Intensity Analysis of the Excited-State Proton-Transfer Dynamics of 2-Hydroxybenzaldehyde in the Charge-Transfer/Proton-Transfer Absorption Band

Xue-Lian Jiang,[†] Ke-Mei Pei,[†] Hui-Gang Wang,[†] Xuming Zheng,*[,†] Wei-Hai Fang,*[,‡] and David Lee Phillips*[,§]

Department of Chemistry and State Key Laboratory of ATMMT(MOE), Zhejiang Sci-Tech University, Hangzhou 310018, People's Republic of China, Department of Chemistry, Beijing Normal University, Beijing 100875, People's Republic of China, and Department of Chemistry, The University of Hong Kong, Pokfulam Road, Hong Kong SAR, People's Republic of China

Received: June 28, 2007; In Final Form: October 7, 2007

Resonance Raman spectra were obtained for 2-hydroxybenzaldehyde (OHBA) in cyclohexane solution with excitation wavelengths in resonance with the first charge-transfer/proton-transfer (CT/PT) band absorption. These spectra indicate that the Franck−Condon region photodissociation dynamics have multidimensional character with motion predominantly along the nominal C═CH in-plane bend + ring deformation modes (ν_9, ν_{10}, ν_{14}, ν_{16}, ν_{18}, ν_{19}, ν_{20}, ν_{26}, ν_{30}, ν_{31}, and ν_{35}) accompanied by a smaller amount of motion along the nominal C═O stretch mode (ν_7), the nominal C═C−C(═O) in-plane bend modes (ν_{33} and ν_{37}), and the nominal ring C−O−H in-plane bend modes (ν_9 and ν_{14}). A preliminary resonance Raman intensity analysis was done, and these results for the OHBA molecule were compared to results previously reported for the 2-hydroxyacetophenone (OHAP) molecule. Several proton-transfer tautomers in the ground and excited states were predicted from the results of B3LYP/cc-PVTZ, UB3LYP/cc-PVTZ, and CASSCF/cc-PVDZ level of theory computations. The differences and similarities between the CT/PT band resonance Raman spectra and the vibrational reorganizational energies for the OHBA molecule relative to those for the OHAP molecule are briefly discussed.

Introduction

Since Weller discovered the excited-state intramolecular proton-transfer (ESIPT) reaction of methyl salicylate (MS),[1] ESIPT reactions have been observed to play an important role in many chemical and biological systems.[2−4] ESIPT reactions have also found many important applications in laser materials,[5−7] in information storage devices and optical switching,[8−10] in hard-scintillation counters,[11] and as polymer photostabilizers.[12,13] A number of experimental and theoretical studies have investigated the types of ESIPT reactions[14−16] and the subsequent complicated reaction mechanisms[17−42] that may take place for a range of molecular systems. Many aspects of the reaction mechanisms of ESIPT processes in a variety of chemical and biological species have been elucidated by various time-resolved spectroscopic measurements and quantum mechanical studies. The ESIPT reaction rates (or the time required for conversion of the enol to its keto tautomer) have been measured using a variety of ultrafast laser spectroscopy methods, and these experiments have shown that the rates of reaction can be very fast (most of them are within 100 fs).[17−25] For example, femtosecond fluorescence depletion experiments determined a 60 ± 10 fs lifetime for methyl salicylate.[19] Similarly, ultrafast pump−probe spectroscopic studies determined ESIPT time constants of 35 fs for 3-hydroxyflavone in methyl cyclohexane or acetonitrile solutions (and a 60 fs time constant in ethanol solution[20]), 55 fs for 2-(2′-hydroxy phyenyl)benzothiazole (HBT) in cyclohexane solution,[22] ∼100 fs for 2-(2′-hydroxy-5′-methyl phenyl)-benzotriazole in nonpolar solvents,[23] less than 50 fs for [2,2′-bipyridyl]3,3′-diol,[24] and 110 ± 15 fs for 2,5-bis(2′-benzoxazolyl) hydroquinone in tetrahydrofuran.[25] Very fast ESIPT reactions have also prompted a number of theoretical and computational studies to gain further insight into their basic mechanisms and possible methods for controlling ESIPT reactions.[26−32] Subsequent reactions taking place after ESIPT were also studied for several molecules. For example, Mitra and Mukherjee[33] studied the ESIPT photophysical properties of 4-methyl-2,6-diformylphenol and 4-methyl-2,6-diacetylphenol using time-resolved fluorescence spectroscopy and ab initio calculations. This work found that the ultrafast ESIPT process was followed by a rapid intramolecular vibrational relaxation (IVR) with a time constant of few picoseconds before fluorescence emission occurred from their keto tautomer on the excited-state potential energy surface.[33] Cho et al. investigated the relaxation processes of the excited-state intramolecular reverse proton transfer (r-ESIPT) in the excited triplet state of 1-hydroxyanthraquinone by using transient Raman spectroscopy and ab initio calculations.[34] Stock et al. studied the ESIPT reaction and the subsequent internal conversion (IC) of the 2-hydroxybenzaldehyde (OHBA) molecule by employing transient absorption measurements with 30 fs time resolution and quantitative fluorescence spectroscopy.[35] They showed that IC proceeds via a thermally activated process over an energy barrier of about 200 meV caused by an avoided crossing between the $\pi\pi^*$ and $\pi\sigma^*$ states.

Resonance Raman intensity analysis (RRIA) studies have been reported for the ESIPT reactions of 2-hydroxyacetophenone (OHAP)[36] and 2-nitrophenol (ONP)[37] and for the photochemical

* Authors to whom correspondence should be addressed. Fax: 86-0571-86843223 (X.Z.); 852-2857-1586 (D.L.P.). E-mail: zhengxuming126@126.com; phillips@hkucc.hku.hk.
[†] Zhejiang Sci-Tech University.
[‡] Beijing Normal University.
[§] The University of Hong Kong.

10.1021/jp0750506 CCC: $37.00
Published on Web 11/22/2007

reactivity of some nucleobases.[38−40] The results reveal that ESIPT reactions evolve rapidly along a large number of skeletal coordinates and without including substantial O−H stretch motion initially.[36−37] These studies also showed that the vibrational reorganizational energies for these molecules vary significantly from one another and indicate that their ESIPT dynamics are very different in terms of the geometry structural changes that initially take place.[36,37] The differences in the photochemical reactivity between thymine and uracil have been correlated with their very different vibrational reorganization energy distribution among the various modes in these molecules, especially among the photochemically relevant modes.[38−40]

OHBA is the smallest aromatic molecule displaying ESIPT and is an attractive prototypical molecular system to study. Theoretical studies on OHBA have predicted a small[32] or nonexistent barrier[41−42] for the proton transfer and suggested that similar reaction dynamics may occur for many other ESIPT systems. The ESIPT was found to take place in less than 50 fs over the whole absorption range of the $S_1(\pi\pi^*)$ state for both OHBA and its monodeuterated analogue, and this suggests that there is either a very small or nonexistent barrier to reaction.[18] The excited-state geometry structural dynamics for the OHBA molecule have not yet been reported to our knowledge. In this paper, we report a preliminary resonance Raman intensity analysis study of the short-time ESIPT dynamics of OHBA in its charge-transfer/proton-transfer (CT/PT) absorption band. Resonance Raman spectra and absolute Raman cross-section measurements were obtained with 319.9 and 341.5 nm excitation wavelengths, and these data were then simulated using time-dependent wave packet calculations employing a simple model. Density functional theory and complete active space self-consistent field (CASSCF) computations have been carried out to predict the ground-state and the excited-state proton-transfer isomerization reactions for OHBA. The results for OHBA obtained here are compared to results obtained from previous studies of OHAP to examine the differences and/or similarities in their Franck−Condon region dynamics.

Experimental and Computational Methods

A. Resonance Raman experiments. The methods and experimental apparatus used for the resonance Raman experiments have been described elsewhere,[43−50] so only a short account will be given here. The harmonics of a nanosecond Nd:YAG laser and their hydrogen Raman shifted laser lines were used to generate the 319.9 and 341.5 nm excitation wavelengths employed in the resonance Raman experiments. The solution-phase samples used concentrations of approximately 0.003−0.010 M OHBA (99% purity) in spectroscopic grade cyclohexane (99.5+% purity) solvent. The power dependent on the resonance Raman spectra was tested (Figure S1 in Supporting Information), and a lower power was used during the resonance Raman measurements to avoid saturation effects and other problems associated with high peak powers. Depletion of the ground-state species could lead the Raman band intensities of the sample relative to those of the solvent to changes as the laser power increases. High peak power can also produce more photochemical intermediates or cause the two-photon ionization processes to occur during the laser pulse. These may possibly interfere with the absolute Raman cross-section measurements. The excitation laser beam used a $\sim$100 μJ loosely focused to a 0.5−1.0 mm diameter spot size onto a flowing liquid stream of sample so as to ensure that all of the Raman peaks belong to the OHBA compound. A backscattering geometry was used for sample excitation and for collection of the Raman scattered light by reflective optics that imaged the Raman scattered light through a polarizer and entrance slit of a 0.5 m spectrograph. The grating of the spectrograph dispersed the light onto a liquid nitrogen cooled charge coupled device (CCD) mounted on the exit of the spectrograph, and the CCD acquired the Raman signal for about 90−120 s before being read out to an interfaced personal computer. About 10−30 of these scans were summed to obtain the resonance Raman spectrum. The Raman shifts of the resonance Raman spectra were calibrated using the known vibrational frequencies of the cyclohexane solvent Raman bands. The solvent Raman bands were subtracted from the resonance Raman spectra using an appropriately scaled solvent spectrum. Spectra of an intensity calibrated deuterium lamp were used to correct the resonance Raman spectral intensities for the variation in the detection efficiency as a function of wavelength. Sections of the resonance Raman spectra were fit to a baseline plus a sum of Lorentzian bands to obtain the integrated areas of the Raman bands. The absolute Raman cross-sections of the OHBA resonance Raman spectra were determined relative to the absolute Raman cross-sections of the 802 cm^{-1} Raman band of the cyclohexane solvent, and the depolarization ratio ρ of the all Raman fundamental for OHBA was estimated to be $^1/_3$ because the A-band absorption is mainly a single nondegenerate electronic state that is well-separated from the B-band absorption. (For details, see discussion in the Results and Discussion section.) The Fourier transform (FT) IR and FT-Raman spectra of OHBA in the neat solid phase were acquired to help assign the resonance Raman spectra.

B. Time-Dependent Wave Packet Calculations To Model the Resonance Raman Intensities and Absorption Spectrum. The absorption spectrum and resonance Raman intensities were modeled using Heller's time-dependent wavepacket approach to resonance Raman scattering[51−54] with the absorption spectrum calculated using the following expression

$$\sigma_A(E_L) = (4\pi e E_L M_0^2/3n\hbar c) \int_{-\infty}^{\infty} G(\delta)\, d\delta\ \mathrm{Re} \int_0^{\infty} dt\, \langle 0|0(t)\rangle \exp[i(E_L + \epsilon_0)]t/\hbar] \exp[-\Gamma t/\hbar]$$

and the resonance Raman intensities were calculated using the following formula

$$\sigma_R(E_L) = (8\pi e^4 E_S^3 E_L M_0^4/9\hbar^6 c^4) \int_{-\infty}^{\infty} G(\delta)\, d\delta\ |\int_0^{\infty} dt\, \langle f|0(t)\rangle \exp[i(E_L + \epsilon_0)]t/\hbar] \exp[-\Gamma t/\hbar]|^2$$

where E_L is the incident photon energy, M_0 is the transition length evaluated at the equilibrium geometry, f is the final state for the Raman scattering, and n is the solvent index of refraction. The term $\exp[-\Gamma t/\hbar]$ is a homogeneous damping function that has contributions from the excited-state population decay and pure dephasing. $G(\delta)$ is some normalized inhomogeneous distribution of electronic zero−zero frequency shifts centered at $\delta = 0$, usually taken to be Gaussian. $|0(t)\rangle = e^{-iHt/\hbar}|0\rangle$, which is $|0\rangle$ propagated on the excited-state surface for a time t, and H is the excited-state vibrational Hamiltonian.

The ground- and excited-state potential energy surfaces were simulated using harmonic oscillators with their minima set apart by an amount Δ (with dimensionless units for the ground-state normal coordinates). The simple model used here did not employ Duschinsky rotation[53,54] of the normal modes, and the ground- and excited-state harmonic oscillators had the same vibrational frequency. The resonance Raman intensities of the first several overtones as well as the combination bands and the absorption spectrum are determined mainly by the slope of the excited-

state surface in the Franck−Condon region in the absence of any vibrational recurrences, and the featureless solution-phase A-band absorption spectra of OHBA suggests that the total electronic dephasing and/or population decay occurs before the first vibrational recurrence of any Franck−Condon active modes. For the resonance Raman bands observed in our experimental spectra, the $\langle f|\ I(t)\rangle$ overlaps decay and have a negligible value after about 30 fs, and the effects of solvent dephasing used a simple exponential decay term ($\exp[-t/\tau]$). OHBA displayed a barrierless or nearly barrierless proton-transfer reaction. Thus the bound harmonic oscillator model used here only provides a convenient method to simulate the Franck−Condon region portion of the excited-state surface that determines the resonance Raman intensities and absorption spectrum and does not in any way imply that the excited state is actually bound.

C. Density Functional Theory and CASSCF Computations. Density functional theory (DFT) and CASSCF calculations[55−57] were done to determine the optimized geometry and vibrational frequencies as well as the electronic transition energies for the ground or excited electronic states of OHBA. Complete geometry optimization and vibrational frequency determination were computed by using the B3LYP/cc-PVTZ level of theory for the ground state of OHBA and the CASSCF-(10,8)/cc-PVDZ level of theory for the excited-state of OHBA, respectively, and employing a C_s symmetry constraint. The electronic transition energies were calculated using the B3LYP-TD/cc-PVTZ level of theory. To describe the low-lying electronic states of OHBA and OHAP, the active orbitals were chosen according to the B3LYP-TD/cc-PVTZ orbital transition calculations and the description of the localized molecular orbital. The three π and three π^* orbitals on the molecule should be used as the active orbitals for the CASSCF calculations. In addition, the two oxygen nonbonding orbitals are also included in the active space. This leads to an active space with 10 electrons in 8 orbitals and is referred to as CASSCF(10,8) hereafter. All of the transition state structures computed were confirmed by using intrinsic reaction coordinate (IRC) methods. All of the DFT and CASSCF calculations made use of the Gaussian program software suite.[58]

Results and Discussion

A. Ground-State Proton-Transfer Isomerization Reactions. 2-Hydroxybenzaldehyde has two possible primary intramolecular proton-transfer isomers in the ground electronic state called the facial keto tautomer FK(S_0) and the backward keto tautomer BK(S_0). Density functional theory calculations were done to determine their global minimum structures. While the backward tautomer was found to have a direct primary proton transfer, the facial tautomer does not exist on both the B3LYP/cc-PVTZ or the MP2/cc-PVTZ potential energy surfaces. We note that a previous study using the HF/6-31+G-(df,pd) level of theory for the ground-state proton-transfer isomerization of OHBA predicted the facial tautomer as a global minimum structure but not the backward tautomer.[30] The discrepancy between the results obtained from our present B3LYP/cc-PVTZ or MP2/cc-PVTZ calculations and the previously reported HF/6-31+G(df,pd) computations can be ascribed mostly to the differences in the level of theory used in the computations. According to results from previous theoretical studies, the calculation of intramolecular hydrogen-bonding systems at the Hartree−Fock (HF) levels may not be accurate enough to predict the details of molecular properties such as the geometrical and conformational features.[59−61] However, DFT methods have been found to provide excellent agreement with available experimental data for benzene derivatives containing hydrogen bonding.[62−64] We thus expect that the results obtained using DFT or MP2 computations would be more reliable than those from lower level of theory HF calculations.

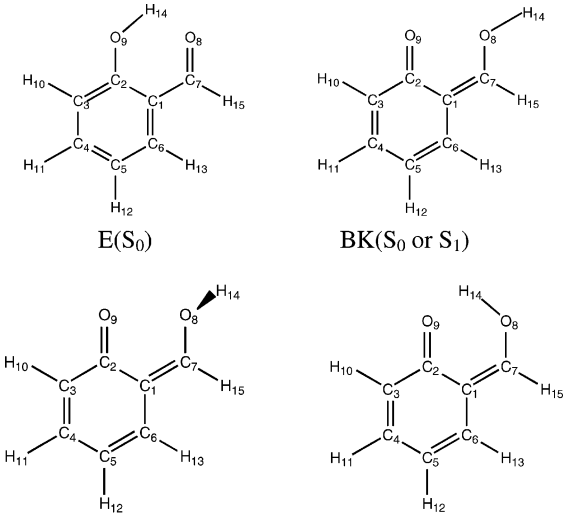

Figure 1. Schematic diagrams for the structures of the ground state of 2-hydroxybenzaldehyde (OHBA) in enol form E(S_0), its ground-state proton-transfer tautomers of the facial keto form FK(S_0) and in the backward keto form BK(S_0), the ground-state transition state TS-(E-BK) between E(S_0) and BK (S_0), its first singlet excited-state proton-transfer tautomers of the facial keto form FK(S_1) and the backward keto form BK(S_1), as well as its first triplet excited-state proton-transfer tautomers of the facial keto form FK(T_1), the backward keto form BK-(T_1), and the corresponding transition state TS(FK−BK)(T_1) between FK(T_1) and BK(T_1). See Table 1 for more detailed structural parameters.

Figure 1 shows simple diagrams of the structures for the ground-state OHBA molecule and its proton-transfer tautomers. By using the synchronous transit-guided quasi-Newton (STQN) method and the B3LYP/cc-PVTZ level of theory computations, the transition state structure (TS(E-BK)(S_0)) between the ground-state OHBA (E(S_0)) and its backward tautomer (BK(S_0)) was determined, and its computed structure is also shown in Figure 1. BK(S_0) is energetically 30.5 kcal/mol higher than E(S_0). Table 1 lists the B3LYP/cc-PVTZ computed geometry parameters for E(S_0), BK(S_0), and TS(E-BK)(S_0). The structural parameters found for E(S_0) and BK(S_0) are noticeably different from one another. The C_1-C_2 and C_7-O_8 bond lengths of BK(S_0) were found to be more than 0.07 Å longer than those of E(S_0), and the C_2-O_9 and C_1-C_7 bond lengths of BK(S_0) are about 0.1 Å shorter than those of E(S_0). These four bonds undergo the largest changes when the ground-state proton-transfer tautomerization reaction takes place. The other C−C bond length changes for E(S_0) are moderate and within about 0.03−0.06 Å longer or shorter than those of BK(S_0). All of the bond angle changes are within p±4°. While the geometry structural parameters of TS(E-BK)(S_0) are very different from those of E(S_0), they are in general very similar to those of BK(S_0) except for the C_7-H_{15} and O−H bonds that are distorted away from the benzene ring plane. The barrier height for the transition from E(S_0) to BK(S_0) was determined to be 37.2 kcal/mol.

B. Discussion of Absorption Spectra. Figure 2 displays the absorption spectrum of OHBA in cyclohexane solution with the excitation wavelengths for the resonance Raman experiments indicated above the spectrum. There are three experimental absorption bands with maxima at about 330, 259/252, and 215 nm (typically called the A-, B-, and C-bands respectively) in Figure 2. Table 2 lists the B3LYP-TD/cc-PVTZ computed

TABLE 1: B3LYP/cc-PVTZ and CASSCF(8,7)/cc-PVDZ Computed Bond Lengths (Å) and Bond Angles (deg) for Various Ground and Excited-State Proton-Transfer Tautomers and Proton Rotamers of OHBA and Their Corresponding Transition States[a]

	S_0			T_1			S_1		
parameters	$E(S_0)$	$BK(S_0)$	$TS(E\text{-}BK)(S_0)$	$FK(T_1)$	$BK(T_1)$	$TS(FK-BK)(T_1)$	$FK(S_1)$	$BK(S_1)$	$TS(FK-BK)(S_1)$
R_{C1-C2}	1.42	1.49	1.50	1.48	1.50	1.48	1.45	1.43	1.43
R_{C2-C3}	1.40	1.46	1.46	1.43	1.43	1.43	1.43	1.37	1.37
R_{C3-C4}	1.38	1.35	1.35	1.40	1.40	1.40	1.46	1.41	1.41
R_{C4-C5}	1.40	1.44	1.44	1.38	1.38	1.38	1.35	1.39	1.39
R_{C5-C6}	1.38	1.35	1.35	1.42	1.42	1.42	1.47	1.39	1.39
R_{C6-C1}	1.40	1.44	1.45	1.40	1.39	1.38	1.37	1.42	1.42
R_{C1-C7}	1.45	1.36	1.35	1.41	1.41	1.42	1.46	1.41	1.42
R_{C7-O8}	1.23	1.33	1.35	1.34	1.35	1.36	1.31	1.35	1.36
R_{O8-H14}	1.75	0.96	0.96	0.99	0.96	0.96	0.97	0.94	0.95
R_{C2-O9}	1.34	1.23	1.22	1.27	1.25	1.25	1.24	1.34	1.34
R_{C3-H10}	1.08	1.08	1.08	1.08	1.08	1.08	1.08	1.08	1.08
R_{C4-H11}	1.08	1.08	1.08	1.08	1.08	1.08	1.08	1.08	1.08
R_{C5-H12}	1.08	1.08	1.08	1.08	1.08	1.08	1.08	1.08	1.08
R_{C6-H13}	1.08	1.08	1.08	1.08	1.08	1.08	1.08	1.08	1.08
R_{C7-H15}	1.10	1.09	1.09	1.08	1.08	1.08	1.08	1.08	1.08
$\angle_{C1-C2-C3}$	119	115	115	119	117	117	116	121	121
$\angle_{C2-C3-C4}$	120	122	122	122	123	123	123	121	120
$\angle_{C3-C4-C5}$	122	122	122	119	119	119	120	120	120
$\angle_{C4-C5-C6}$	119	120	120	122	121	121	118	120	120
$\angle_{C5-C6-C1}$	121	121	121	122	123	122	123	122	122
$\angle_{C6-C1-C2}$	120	120	119	117	117	118	121	117	117
$\angle_{C2-C1-C7}$	120	123	123	120	124	122	121	124	123
$\angle_{C1-C2-O9}$	122	123	123	121	122	122	121	120	120
$\angle_{C3-C2-O9}$	119	122	122	121	120	120	124	119	119
$\angle_{C1-C7-O8}$	125	124	125	124	123	123	123	121	123
$\angle_{C7-O8-H14}$		109	113	106	109	113	108	110	111
$\angle_{C1-C7-H15}$	116	119	119	122	119	120	122	121	120
$\angle_{O8-C7-H15}$	120	116	116	115	117	117	116	118	117
$\angle_{C2-C3-H10}$	119	116	116	116	116	116	117	119	119
$\angle_{C4-C3-H10}$	122	122	122	122	121	121	120	120	121
$\angle_{C3-C4-H11}$	119	120	120	121	121	120	119	119	119
$\angle_{C5-C4-H11}$	119	118	118	121	121	121	121	121	121
$\angle_{C4-C5-H12}$	120	119	119	120	120	120	123	121	120
$\angle_{C6-C5-H12}$	121	121	121	118	119	119	119	120	120
$\angle_{C5-C6-H13}$	120	120	121	119	118	119	118	120	120
$\angle_{C1-C6-H13}$	119	118	118	120	119	119	119	118	118
$D_{C1-C7-O8-H14}$	0°	180°	104.3°	0°	180°	−90.4°	0°	−164.3°	−90.6°

[a] See text for more details.

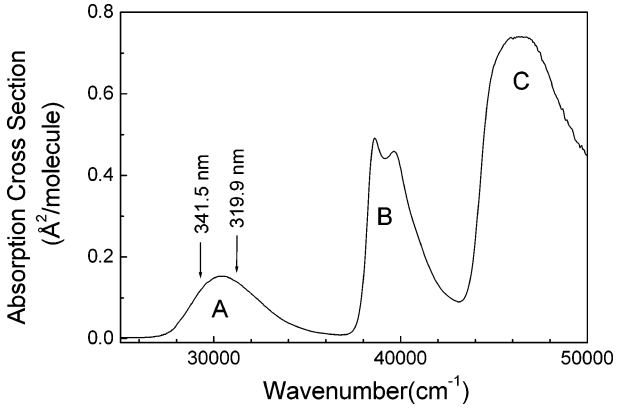

Figure 2. UV absorption spectra of OHBA in cyclohexane solution is shown. The excitation wavelengths used for the resonance Raman experiments are indicated above the absorption spectrum.

TABLE 2: B3LYP-TD/cc-PVTZ Calculated Transition Energies of OHBA

states (Cs)	character	singlet transition energies calcd.	singlet transition energies exptl.	oscillator strength *f* calcd.	oscillator strength *f* exptl.	orbitals
2-Hydroxybenzaldehyde						
$S_1(1A')$	$^1(\pi,\pi^*)$	315 nm	330 nm	0.0640	0.0667	32 → 33
$S_2(1A'')$		314 nm		0.0002		31 → 33
$S_3(2A')$	$^1(\pi,\pi^*)$	242 nm	259/252 nm	0.1589	0.1683	30 → 33
$S_4(3A')$	$^1(\pi,\pi^*)$	212 nm	218 nm	0.1885	0.2596	32 → 34
$S_5(2A'')$		201 nm		0.0004		31 → 34
2-Hydroxyacetophenone						
$S_1(1A')$	$^1(\pi,\pi^*)$	317 nm		0.0823		36 → 37
$S_2(1A'')$		310 nm		0.0002		35 → 37
$S_3(2A')$	$^1(\pi,\pi^*)$	243 nm		0.1469		34 → 37
$S_4(3A')$	$^1(\pi,\pi^*)$	210 nm		0.1066		36 → 38
$S_5(2A'')$		201 nm		0.0000		35 → 38

electronic transition energies, the corresponding orbitals, and the oscillator strengths. The calculated results show that among the calculated electronic transitions with wavelengths longer than 200 nm there are three transition-allowed absorption bands at 315, 242, and 212 nm that have oscillator strengths of $f = 0.0640$, 0.1589, and 0.1885, respectively. This is in a good agreement with the three intense experimental absorption bands at 330 nm ($f = 0.0667$), 259/252 nm ($f = 0.1683$), and 218 nm ($f = 0.2596$), respectively, for OHBA. The A-band absorption of OHBA is located at 330 nm and is clearly separated from the B-band at 259/252 nm. The A-band absorption (330 nm) is mostly a single, nondegenerate electronic state, which is assigned to a π (benzene ring + OH) → π^*(benzene ring + C=O) transition on the basis of our time-dependent (TD)-DFT computations and natural orbital analysis results. The corresponding π orbital 32 (HOMO) and π^* orbital 33 (LUMO) for the electronic transition of the 330 nm A-band of OHBA are

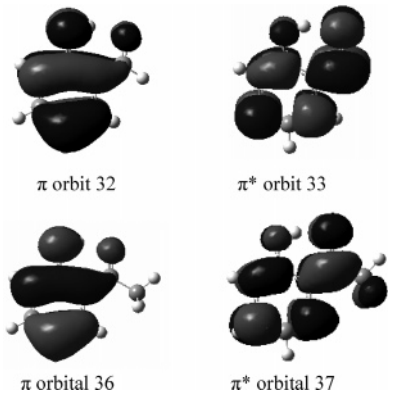

Figure 3. Diagram of the molecular orbitals involved in the electronic transition for the A-band absorption of OHBA (e.g., orbitals 32 and 33) and OHAP (e.g., orbitals 36 and 37).

displayed in Figure 3. The electronic orbitals that are involved in the B- and C-band absorptions are π orbital 30 (HOMO − 2) and π^* orbital 33 (LUMO) and π orbital 32 (HOMO) and π^* orbital 34 (LUMO + 1), respectively (Figure S2 in the Supporting Information). Figure 3 shows that while orbital 32 has its electron density mostly delocalized into the benzene ring and the OH groups orbital 33 has its electron density more delocalized into the benzene ring and the HC═O groups. This endows the A-band absorption with a CT/PT character and suggests that more electron density will flow from the OH moiety into the HC═O moiety and cause the electron density to increase or decrease considerably for the HC═O or OH groups upon photoexcitation. The obvious dependence of the A-band absorption spectrum of OHBA on the solvent polarity (this work) is consistent with its CT/PT character. It appears that our 341.5 and 309.1 nm excitation wavelengths used in the resonance Raman experiments should be mostly in resonance with the A-band absorption of OHBA. The depolarization ratio $\rho = {}^1/_3$ was used for the absolute Raman cross-section measurements of all bands observed in our 341.5 and 309.1 nm resonance Raman spectra. This is based on the selection rule that the depolarization ratio ρ should be ${}^1/_3$ for all bands if the Raman intensity derives solely from a single, nondegenerate electronic state in liquids at room temperature.[54] Because the CT/PT absorption band at 330 nm is strong and well-separated from the other two absorption bands, this appears to be a reasonable approximation.

C. Resonance Raman Spectra. Figure 4 shows an overview of the A-band resonance Raman spectra of OHBA obtained with 341.5, 319.9, 252.7, and 217.8 nm excitation wavelengths. While 341.5 and 319.9 nm resonance Raman spectra are very similar to each other, the 252.7 and 217.8 nm resonance Raman spectra display a very different intensity pattern than the 341.5 and 319.9 nm resonance Raman spectra. It is interesting to note that the most intense vibrational modes in the 252.7 and 217.8 nm resonance Raman spectra are 1667 and 1615 cm^{-1}, respectively, which become much weaker in the 341.5 and 319.9 nm resonance Raman spectra, especially for the 1615 cm^{-1} vibrational mode. Thus we expect that the preresonance interference to the A-band from a higher-lying state (B- or C-band) is very limited. Figure 5 presents an expanded view of the resonance Raman spectrum obtained with 341.5 nm excitation with tentative vibrational assignments indicated above the spectrum. The notations and assignments of the vibrations are based on our FT═Raman, FT-IR, and B3LYP/cc-PVTZ computations (Figure S3 and Table S1 in the Supporting Information) and are similar to those reported in ref 65. The spectra shown in Figures 4 and 5 have been corrected for sample reabsorption as

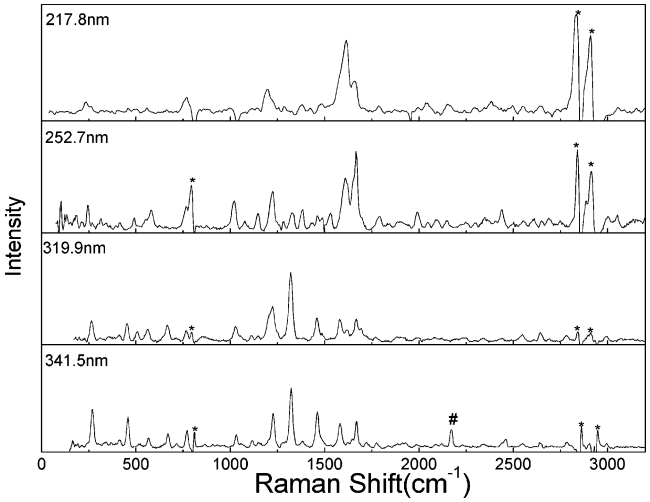

Figure 4. Overall view of the A-band resonance Raman spectra of OHBA in cyclohexane solvent obtained with the excitation wavelengths (in nm) indicated next to each spectrum. The spectra have been intensity corrected and solvent subtracted. (Asterisks mark regions where solvent subtraction artifacts are present; the sharp feature labeled by the pound sign is due to a stray laser line.) The actual concentrations used are about 0.044 and 0.051 mol/L for 341.5 and 319.9 nm excitations, and the corresponding relative intensities between the OHBA 668 cm^{-1} peak and the cyclohexane 802 cm^{-1} peak are 0.27 and 0.44, respectively.

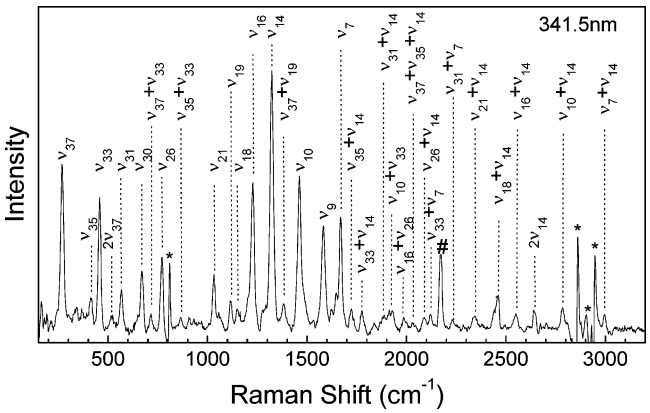

Figure 5. Expanded view of the 341.5 nm resonance Raman spectrum of OHBA in cyclohexane. The spectrum has been intensity corrected and solvent subtracted. Asterisks label parts of the spectrum where solvent subtraction artifacts are present. The tentative assignments to the larger Raman band features are also shown.

well as the wavelength dependence response of the detection system, and the solvent Raman bands were removed from the spectra by subtracting an appropriately scaled solvent spectrum, and regions of the solvent subtraction artifacts are indicated by asterisks. We note that the intensity of some Raman bands in the spectrum may have contributions from several Raman bands that have very close Raman shifts due to the limited resolution of the solution-phase spectra, and therefore the Raman band labels in Figure 5 only indicate the largest Raman band contributions to each Raman band observed. Most of the resonance Raman bands can be assigned to the fundamentals, overtones, and combination bands of about 14 Franck−Condon active vibrations based on the vibrational assignments of OHBA (our work based on FT-Raman/FT-IR experiments and density functional calculations as well as previously reported results in ref 65): the nominal ring C═C−H/C−O−H in-plane bend mode ν_{14} at 1314 cm^{-1}, the nominal ring C═C−H/C−C(═O)−H in-plane bend mode ν_{16} at 1221 cm^{-1}, the nominal C═C−H in-plane bend modes ν_{18}, ν_{19}, and ν_{20} at 1144, 1102, and

TABLE 3: Resonance Raman Intensity Analysis Parameters for the Time-Dependent Wave Packet Calculations and the Resulting Vibrational Reorganization Energies for 2-Hydroxybenzaldehyde

modes	descriptions	freq. (cm^{-1})	$\|\Delta\|$	vibrational reorganization energy
	2-Hydroxybenzaldehyde (OHBA)			
ν_{37}	C═C−C(═) in-plane bend + C═C−C(−OH) in-plane bend	264	1.55	317
ν_{35}	ring deformation + C−O in-plane bend	410	0.55	62
ν_{33}	C═C−O(OH) in-plane bend + C═C−C(═) in-plane bend	453	0.78	138
ν_{31}	ring deformation	562	0.55	85
ν_{30}	ring deformation + C−C(H)═O in-plane	668	0.63	133
ν_{26}	ring deformation	764	0.30	34
ν_{20}	C═CH in-plane bend	1028	0.38	74
ν_{19}	C═CH in-plane bend	1111	0.22	27
ν_{18}	C═CH in-plane bend	1144	0.20	23
ν_{16}	C═CH in-plane bend + C−C(═)-H in-plane bend	1224	0.35	75
ν_{14}	C═CH in-plane bend + C−O−H in-plane bend	1320	0.65	279
ν_{10}	ring deformation	1458	0.38	97
ν_9	ring deformation + C−O−H in-plane bend + C═CH in-plane bend	1580	0.35	97
ν_7	C═O stretch	1668	0.28	65
				total = 1506
	transition length, $M = 0.555$, $E_{00} = 29\,160\ cm^{-1}$, $\Gamma = 470\ cm^{-1}$, G (standard deviation) $= 520\ cm^{-1}$			
	2-Hydroxyacetophenone (OHAP) (from ref 36)			
ν_{44}	C═C−C(═) in-plane bend + C═C−C(−OH) in-plane bend	264	0.89	105
ν_{41}	C═C−O(OH) in-plane bend + C═C−C(═) in-plane bend	434	0.84	153
ν_{38}	ring deformation	562	0.63	112
ν_{36}	ring deformation + C−C(CH_3)═O in-plane bend	622	0.62	120
ν_{32}	ring deformation	842	0.40	67
ν_{25}	C═CH in-plane bend	1031	0.49	124
ν_{24}	C═CH in-plane bend	1067	0.48	123
ν_{23}	C═CH in-plane bend	1128	0.68	261
ν_{21}	C═CH in-plane bend + C−O−H in-plane bend	1218	0.39	93
ν_{20}	C−C(═) stretch	1245	0.38	90
ν_{19}	ring deformation + CH_3 umbrella	1324	1.33	1171
ν_{13}	C═CH in-plane bend + ring C═C stretch	1445	0.35	88
ν_{11}	ring deformation + C−O−H in-plane bend + C═CH in-plane bend	1584	0.41	133
ν_9	C═O stretch	1648	0.45	167
				total = 2808
	transition length, $M = 0.54$, $E_{00} = 28\,380\ cm^{-1}$, $\Gamma = 101\ cm^{-1}$, G (standard deviation) $= 470\ cm^{-1}$			

1019 cm^{-1}, respectively, the nominal C═C−C(═O)/C═C−O(H) in-plane bend modes ν_{37} at 261 cm^{-1} and ν_{33} at 447 cm^{-1}, the nominal ring deformation modes ν_{10}, ν_{26}, ν_{31}, and ν_{35} at 1455, 764, 559, and 410 cm^{-1}, respectively, the nominal ring deformation/C−C(H)═O in-plane bend mode ν_{30} at 662 cm^{-1}, the nominal ring deformation/C−O−H/C═C−H in-plane bend ν_9 at 1576 cm^{-1}, and the nominal C═O stretch ν_7 at 1662 cm^{-1}. We note that the ring deformation and ring C═C−H in-plane bend are distributed among 10 Franck−Condon active modes (ν_9, ν_{10}, ν_{14}, ν_{16}, ν_{18}, ν_{19}, ν_{20}, ν_{26}, ν_{30}, ν_{31}, and ν_{35}) and the proton-transfer or hydrogen-chelating relevant C═C−C(═O)/C═C−O(H) in-plane bend and C═O stretch motions are distributed among two modes (ν_{33} and ν_{37}) and one mode (ν_7), respectively. It appears that photoexcitation of OHBA in its A-band (or CT/PT) absorption band causes larger motions among the ring deformation, C═C−C(═O)/C═C−O(H) in-plane bend, ring C═C−H in-plane bend, and C═O stretch reaction coordinates.

D. Simulation of the Absorption and Resonance Raman Spectra. We have chosen to model the relative intensities of the 341.5 and 319.9 nm resonance Raman spectra because they are clearly mostly in resonance with the CT/PT band absorption. The absorption spectrum and absolute resonance Raman cross-sections were simulated using the time-dependent wavepacket calculations and a simple model described earlier. Table 3 presents the calculated parameters that best fit the absorption spectrum and the intensities of the 341.5 and 319.9 nm resonance Raman spectra for OHBA in cyclohexane solution. To simultaneously fit the absorption bandwidth and the pattern of the resonance Raman intensities, we needed to include a moderate amount of electronic dephasing (the Γ parameter) and a large amount of inhomogeneous broadening (the G parameter) in the calculations. This is similar to previous work on solution-phase OHAP (the OHAP results are also listed in Table 3),[36] where large damping parameters were needed to simultaneously fit the absolute Raman cross-sections, the relative Raman intensity patterns, and the absorption band. This indicates that the population decay/electronic dephasing takes place substantially faster than just wavepacket motion away from the Franck−Condon region. Table 3 shows that while the Gaussian inhomogeneous broadening (the G parameter) of 520 cm^{-1} for OHBA is similar to that of 470 cm^{-1} for OHAP the Lorentzian homogeneous broadening (the Γ parameter) of 470 cm^{-1} for OHBA is much larger than that of 101 cm^{-1} for OHAP. Inhomogeneous broadening arises because there can be a number of different solvation structures in solution leading to a distribution of electronic transition energies and reflects the static interaction between the molecule of interest and the solvent. That both OHBA and OHAP have similar G parameters in cyclohexane solution suggests that both molecules have a similar interaction with the cyclohexane solvent in the ground electronic state. The distinctly different Γ parameters between the two molecules indicate that the two molecules have significantly different homogeneous broadening. The homogeneous broadening comes from both the solvent-induced dephasing and the excited-state population decay in the condensed phase. The contribution of the excited-state population decay to the homogeneous broadening can be determined from its excited-state lifetime. The S_1 state lifetime of OHBA in the gas phase was determined to be less than 50 fs, and this suggests a

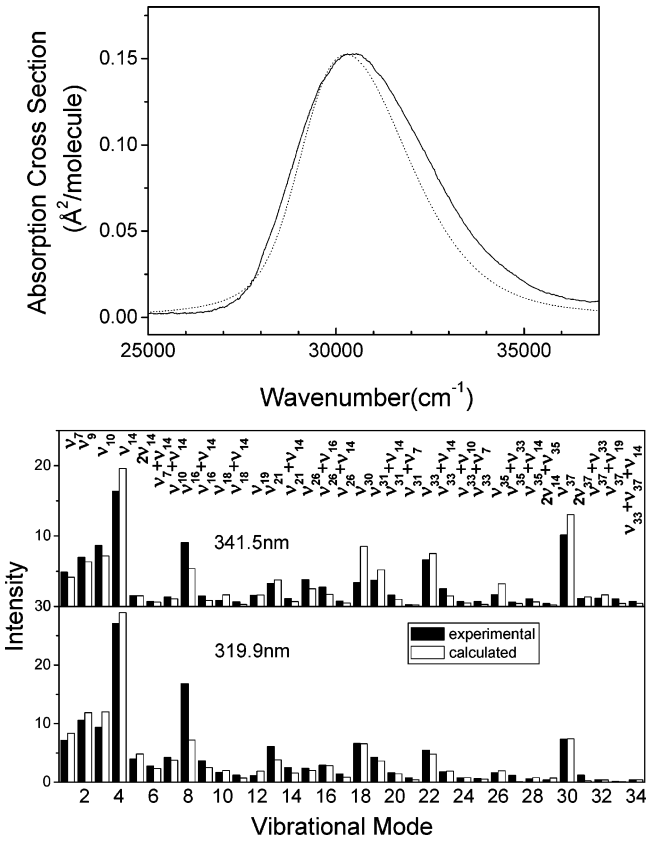

Figure 6. (Top panel) Comparison of the computed absorption spectrum (dotted line) with the experimental (solid line) absorption spectrum. (Bottom panel) Comparison of the computed resonance Raman cross-sections (open bars) with the experimental Raman cross-sections (solid bars) for the main Raman features of the 319.9 and 341.5 nm resonance Raman spectra. The computations made use of the model described in refs 49 and 50 and employed a simple exponential decay dephasing treatment for the solvent. (See text for details.)

line width of a bit more than 100 cm^{-1} ($\tau = 1/2\pi\Gamma c$).[18] Obviously the approximate 100 cm^{-1} line width estimated from the gas-phase excited-state lifetime is much smaller than the homogeneous broadening 470 cm^{-1} line width determined from the solution-phase resonance Raman intensity analysis for OHBA. This suggests that the 470 cm^{-1} homogeneous broadening is possibly composed of the S_1 excited-state lifetime decay and the solvent-induced electronic dephasing. It is likely that the cyclohexane solvent affects both the S_1 state lifetime and the solvent-induced electronic dephasing. Under the extreme case where the 470 cm^{-1} homogeneous broadening is almost entirely derived from the S_1 state lifetime decay, a lower limit of ~10 fs can be inferred for the S_1 state lifetime for OHBA in cyclohexane solution. Therefore, we expect that the S_1 state lifetime of OHBA in cyclohexane solution will be somewhere between 10 and 50 fs. Similarly, using the 101 cm^{-1} homogeneous broadening for OHAP and considering the band shape difference between OHAP and OHBA for their A-band or CT/PT band absorption, the S_1 state lifetime of OHAP is estimated to be longer than 50 fs, and this is in agreement with the gas-phase experimental observation of a 60 fs tautomer rise time for the S_1 state of OHAP.[19]

The top panel of Figure 6 shows a comparison of the calculated absorption spectrum with the experimental absorption spectrum while the bottom panel of Figure 6 and Table 4 show comparisons of the calculated resonance Raman cross-sections (open bars) with the experimental Raman cross-sections (solid bars) for the main Raman features of the 341.5 and 319.9 nm resonance Raman spectra. Inspection of Figure 6 shows that there is reasonable agreement between the calculated and the experimental absorption spectra, and it is worth noting that the calculated spectrum is consistent with the oscillator strength of the CT/PT transition while simultaneously providing a good fit to the absolute Raman intensities of the 341.5 and 319.9 nm spectra as shown in lower part of Figure 6. If any of the parameters in Table 3 are changed beyond their estimated uncertainties (about ±5−10%), then the calculated fit to the absorption spectrum and/or resonance Raman cross-section becomes noticeably poorer. The overall best fit to both the absorption spectrum and the absolute resonance Raman intensities appears reasonable enough to extract the major features of the transition and its associated short-time dynamics on the excited-state potential energy surface. Examination of the $|\Delta|$ dimensionless parameters in Table 3 obtained by fitting the absorption spectrum and the resonance Raman cross-sections shows that the largest changes in the displacements take place with the nominal ring C=C−H/C−O−H in-plane bend mode ν_{14} ($|\Delta| = 0.65$) and the nominal C=C−C(=O)/C=C−O(H) in-plane bend modes ν_{37} ($|\Delta| = 1.55$) and ν_{33} ($|\Delta| = 0.78$). There are also more modest contributions from the other 11 normal modes of the nominal ring deformations, the C=O stretch, and the ring C=C−H in-plane bend. Our results indicate that the short-time photodissociation dynamics of OHBA have significant multidimensional character distributed over a wide variety of vibrational modes.

TABLE 4: Resonance Raman Intensities of OHBA2-Hydroxybenzaldehyde in Cyclohexane Solution

absolute Raman cross-section σ_R ($\times 10^{-10}$ Å/molecule)[a]					
		319.9 nm		341.5 nm	
Raman peaks	Raman shift (cm^{-1})	exptl.	calcd.	exptl.	calcd.
ν_7	1670	7.18	8.36	4.87	4.16
ν_9	1582	10.59	11.87	6.95	6.33
ν_{10}	1461	9.38	12.01	8.65	7.15
ν_{14}	1323	27.07	28.94	16.37	19.59
$2\nu_{14}$	2640	3.97	4.83	1.53	1.51
$\nu_{14} + \nu_7$	2997	2.77	2.36	0.72	0.6
$\nu_{14} + \nu_{10}$	2784	4.24	3.75	1.37	1.06
ν_{16}	1228	16.84	7.2	9.1	5.36
$\nu_{14} + \nu_{16}$	2549	3.66	2.5	1.49	0.84
ν_{18}	1147	1.67	2.04	0.87	1.65
$\nu_{14} + \nu_{18}$	2461	1.24	0.73	0.66	0.27
ν_{19}	1114	1.16	1.92	1.6	1.61
ν_{20}	1032	6.07	3.84	3.28	3.79
$\nu_{14} + \nu_{20}$	2343	2.5	1.58	1.12	0.68
ν_{26}	772	2.4	2.03	3.82	2.5
$\nu_{16} + \nu_{26}$	1986	2.9	2.83	2.74	1.72
$\nu_{14} + \nu_{26}$	2089	1.42	0.84	0.75	0.47
ν_{30}	670	6.61	6.57	3.38	8.52
ν_{31}	567	4.3	3.64	3.74	5.19
$\nu_7 + \nu_{31}$	2228	1.62	1.46	1.61	1.0
$\nu_{14} + \nu_{31}$	1887	0.8	0.42	0.24	0.2
ν_{33}	457	5.46	4.81	6.64	7.51
$\nu_{14} + \nu_{33}$	1775	1.8	1.92	2.51	1.49
$\nu_{10} + \nu_{33}$	1914	0.8	0.8	0.67	0.51
$\nu_7 + \nu_{33}$	2122	0.63	0.54	0.71	0.27
ν_{35}	412	1.63	1.97	1.67	3.19
$\nu_{35} + \nu_{33}$	865	1.19	0.11	0.62	0.41
$\nu_{35} + \nu_{14}$	1723	0.6	0.79	1.08	0.65
$\nu_{35} + 2\nu_{14}$	3049	0.4	0.72	0.4	0.2
ν_{37}	268	7.39	7.4	10.15	13.02
$2\nu_{37}$	515	1.22	0.23	1.11	1.37
$\nu_{37} + \nu_{33}$	719	0.46	0.38	1.14	1.65
$\nu_{37} + \nu_{19}$	1382	0.15	0.11	1.06	0.4
$\nu_{14} + \nu_{37} + \nu_{33}$	2036	0.43	0.46	0.73	0.42

[a] The absolute Raman cross-sections of the 802 cm^{-1} Raman band of the cyclohexane solvent at 319.1 and 341.5 nm excitation are 0.0694 $\times 10^{-10}$ and 0.0502 $\times 10^{-10}$ Å/molecule (see ref 66).

E. CT/PT Absorption Band Short-Time ESIPT Dynamics of OHBA and Comparison to Previous Work on OHAP. 2-Hydroxyacetophenone is a prototypical proton-transfer molecule for which resonance Raman intensity analysis was carried out for its A-band absorption.[36] Fourteen vibrational modes were found to be significantly enhanced with the most intense Raman band being the symmetric stretch of the benzene ring at 1324 cm^{-1}. An absolute Raman intensity analysis indicated that the breadth of the absorption and emission bands in OHAP was due to displacements in 14 vibrational coordinates not including the O−H stretch, and the electronically excited OHAP evolves rapidly in the Franck−Condon region along a large number of skeletal coordinates without involving the O−H stretching coordinate.[36] The Franck−Condon region proton-transfer dynamics of OHBA are similar to that of OHAP (Table 3) in that both molecules have their short-time proton-transfer dynamics being distributed over a wide range of vibrational modes. We note that while OHAP has about 2808 cm^{-1} total vibrational reorganizational energy that is distributed into 14 vibrational modes with the benzene skeletal motions possessing the largest amount of vibrational reorganizational energy, OHBA has only about 1506 cm^{-1} total vibrational reorganizational energy that is partitioned between 14 Franck−Condon vibrational modes with the benzene skeletal modes also having the largest reorganizational energy. The hydroxy (O−H) stretching mode is not observed in the 341.5 and 319.9 nm resonance Raman spectra of OHBA, and this is similar to the resonance Raman results for OHAP. OHAP has been thought to undergo a barrierless proton-transfer reaction in its first excited state.[7,67] This is similar to the TD−DFT calculations that predicted no barrier for the ESIPT reaction of OHBA,[41,42] and the isotope experiment/HF−CIS calculations suggest an upper limit barrier of only 2.4 kcal/mol for the ESIPT reaction of OHBA.[18] The absence of intensity in the hydroxy stretching mode as well as its combination bands with the nominal benzene skeletal modes in the resonance Raman spectrum for both OHBA and OHAP suggests a mechanism for ESIPT in which an overall molecular geometry change comprised of multiple reaction coordinates takes place rather than along a separable single hydroxy stretch reaction coordinate. It is likely that the skeletal motion occurs prior to or concertedly with the exited state proton-transfer reaction taking place in these systems.

Further examination of the normal mode displacements in OHBA and OHAP reveal distinct differences in their Franck−Condon dynamics. We note from Table 3 that most of the normal modes of OHBA have normal mode descriptions very similar to those of OHAP. However, the corresponding vibrational reorganizational energies of OHBA are considerably different from those of OHAP. The most important normal mode that plays a predominant role in the excited-state proton-transfer dynamics of OHBA is the C═C−H +C−O−H in-plane bend vibration (ν_{14} at 1320 cm^{-1}) that has about 279 cm^{-1} vibrational reorganizational energy and accounts for 19% of the total vibrational reorganizational energy. The corresponding C═C−H +C−O−H in-plane bend vibration (ν_{21} at 1218 cm^{-1}) for OHAP however has only 93 cm^{-1} vibrational reorganizational energy and accounts for only 3% of the total vibrational reorganizational energy. In contrast, the most important normal mode that is specific to OHAP and plays a decisive role in the excited-state proton-transfer dynamics of OHAP is the ring deformation + CH_3 umbrella vibration (ν_{19} at 1324 cm^{-1}), and this mode has a 1171 cm^{-1} vibrational reorganizational energy and accounts for 42% of the total vibrational reorganizational energy. The corresponding ring deformation vibration (ν_{10} at 1458 cm^{-1}) for OHBA however has only 97 cm^{-1} vibrational reorganizational energy and accounts for only 6.4% of the total vibrational reorganizational energy. Thus replacement of the H_α atom of the H_α−C═O group of OHBA by the CH_3 group causes OHAP to increase by ~1074 cm^{-1} (= 1171 cm^{-1} − 97 cm^{-1}) in the vibrational reorganizational energy that accounts for ~82% of the total increase of 1302 cm^{-1} (= 2808 cm^{-1} − 1506 cm^{-1}) in the total vibrational reorganizational energy of OHAP. The replacement of the H atom of OHBA by the CH_3 group also causes OHAP to increase its vibrational reorganizational energies along the nominal ring C═C−H in-plane bend vibrational modes (ν_{23}, ν_{24}, and ν_{25}) relative to the corresponding modes (ν_{18}, ν_{19}, and ν_{20}) of OHBA. The subtotal vibrational reorganizational energy of 508 cm^{-1}(= 124 cm^{-1} + 123 cm^{-1} + 261 cm^{-1}) for these three modes (ν_{23}, ν_{24}, and ν_{25}) of OHAP that account for 18% of the total vibrational reorganizational energy is much larger than the subtotal vibrational reorganizational energy of 124 cm^{-1} (= 74 cm^{-1} + 27 cm^{-1} + 23 cm^{-1}) for the corresponding modes (ν_{18}, ν_{19}, and ν_{20}) that make up only 8% of the total vibrational reorganizational energy for OHBA. This causes OHAP to increase by ~384 cm^{-1} (= 508 cm^{-1} − 124 cm^{-1}) in the subtotal vibrational reorganizational energy that makes up 29% of the total increase of 1302 cm^{-1} in the total vibrational reorganizational energy for OHAP. There are two modes that decreased for the vibrational reorganizational energy in OHAP compared to OHBA. The nominal C═C−C(═O)/C═C−O(H) in-plane bend vibrational modes (ν_{33} and ν_{37}) for OHBA have a subtotal vibrational reorganizational energy of 455 cm^{-1} (= 317 cm^{-1} + 138 cm^{-1}) that accounts for 30% of the total vibrational reorganizational energy. This is considerably larger than the corresponding 258 cm^{-1} (= 105 cm^{-1} + 153 cm^{-1}) that makes up only 9% of the total vibrational reorganizational energy for the ν_{41} and ν_{44} modes of OHAP and causes OHAP to experience a decrease of about 197 cm^{-1} in the vibrational reorganizational energy that accounts for 15% of the total increase in the total vibrational reorganizational energy. The distinct differences in their Franck−Condon dynamics between OHBA and OHAP are likely due to the nature of the π^* orbital 37 in Figure 2 that displays an excited-state supraconjugation interaction between the benzene ring and the CH_2 groups. This excited-state supraconjugation interaction as well as the dynamical forces of the proton-transfer motion increases the C═C−H and other in-plane bending motion and causes more vibrational energy to be partitioned into the C═C−H and other in-plane bend motions for the OHAP molecule. It seems that the CH_3 group in OHAP acts as both the damper of the C═C−C(═O) + C═C−O(H) bending motion and the activator of the ring deformation and ring C═C−H in-plane bend motions.

We have noted from the above analysis that the substitution of the H_α atom in the H_α−C═O group by the CH_3 group effectively modulates the Franck−Condon region ESIPT dynamics and the energy partitioning among the various vibrational degrees of freedom of OHBA. During the ESIPT process, OHAP receives about 2808 cm^{-1} total vibrational reorganizational energy among which more vibrational reorganizational energy is partitioned into the benzene-ring-related ring deformation or C═C−H in-plane bending modes, while OHBA has only a 1506 cm^{-1} total vibrational reorganizational energy in which more vibrational reorganizational energy is distributed along the ESIPT-relevant C−C═O/C−O−H bending modes.

F. Roles of Tautomers and Rotamers on the ESIPT Reaction Path of OHBA. The geometry structures of the excited-state proton-transfer tautomers and proton rotamers of

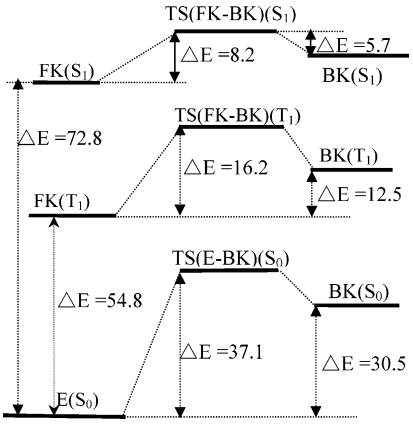

Figure 7. Energies computed for the various proton-transfer tautomers and proton rotamers of OHBA in several electronic states. The denotations are given in Figure 1. See text for more details.

OHBA were calculated using CASSCF(10,8)/cc-PVDZ for the S_1 or $^1(\pi,\pi^*)$ state and UB3LYP/cc-PVTZ for the T_1 or $^3(\pi,\pi^*)$ state. The energetics for the S_1 state were also estimated using CASMP2/cc-PVDZ single-point energy calculations. These calculation results are shown in Figures 1 and 7 and also listed in Table 1. Figure 7 schematically depicts the partial potential energy surface diagram for the ESIPT processes. Figure 1 shows that the OHBA molecule in its S_1 or T_1 excited state has both the facial keto tautomer FK(S_1) or FK(T_1) and the backward keto tautomer BK(S_1) or BK(T_1) in the C_s point group. This is different from the ground-state OHBA molecule that has only a backward proton-transfer tautomer BK(S_0) but without facial keto tautomer FK(S_0).

The structural parameters of FK(S_1) are noticeably different from those of E(S_0). Table 1 shows that the C_3-C_4, C_5-C_6, C_7-O_8, and C_2-O_9 bond lengths for FK(S_1) are 1.46, 1.47, 1.32, and 1.24 Å, which are considerably longer or shorter than the corresponding 1.38, 1.38, 1.23, and 1.34 Å of E(S_0) by more than +0.07, +0.09, +0.09, and −0.10 Å, respectively. These four bonds undergo the largest geometry changes when the excited-state proton-transfer takes place and the excited-state molecule reaches its energy minimum. The $O_9-C_2-C_3$ bond angle of FK(S_1) is 124° and larger than that of E(S_0) by 5°. The other four bond length changes in the C_1-C_2, C_2-C_3, C_4-C_5, and C_6-C_1 bonds and the seven bond angle changes in the $C_2-C_3-H_{10}$, $C_4-C_3-H_{10}$, $C_3-C_4-H_{11}$, $C_5-C_4-H_{11}$, $C_4-C_5-H_{12}$, $C_6-C_5-H_{12}$, and $C_6-C_5-H_{12}$ angles are within ±0.03 Å and ±3°, respectively, for FK(S_1) and E(S_0). The structural parameters listed in Table 1 for BK(T_1), FK(T_1), and TS(FK−BK)(T_1) are very similar to one another with most of the bond length and bond angle changes being less than ±2 Å and ±2°. The structural parameters of FK(S_1) are surprisingly similar to those of TS(FK−BK)(T_1).

On the basis of the CASMP2/cc-PVDZ single-point energy calculations, the FK(S_1) is 72.8 kcal/mol higher in energy than E(S_0) and can undergo further isomerization through a O_8-H_{14} rotation around the C_7-O_8 bond to form BK(S_1) that is energetically only 2.5 kcal/mol higher than FK(S_1). The transition barrier for FK(S_1) to BK(S_1) is 8.2 kcal/mol based on results from the CASMP2/cc-PVDZ single-point energy calculations. This indicates that the further rotamerization from FK(S_1) to BK(S_1) is relatively difficult. Our UB3LYP/cc-PVTZ calculations predict two minimum triplet state structures, FK(T_1) and BK(T_1), and the transition state structure TS(FK−BK)(T_1) for OHBA. Figure 7 shows that BK(T_1) is higher in energy than FK(T_1) by 12.5 kcal/mol, while TS(FK−BK)(T_1) is only 3.7 kcal/mol above BK(T_1) in energy. This indicates that in the first triplet excited state the proton rotamerization reaction from BK(T_1) to FK(T_1) is much easier than the reverse process from FK(T_1) to BK(T_1). The energy difference between FK(S_1) and TS(FK−BK)(T_1) is only 1.8 kcal/mol. This small energy difference and the very similar structural parameters between FK(S_1) and TS(FK−BK)(T_1) lead us to expect that the reverse ESIPT reaction from FK(S_1) and TS(FK−BK)(T_1) exists for OHBA similar to the reverse ESIPT channel for 1-hydroxyanthraquinone.[34] This hypothesis is supported by previous phosphorescence spectroscopic results for the triplet state proton-transfer tautomers in OHBA,[68] in 2-(2′-hydroxyphenyl)-benzoxazole,[69,70] in 2-(2′-hydroxyphenyl)benzothiazole,[71] and in 2,2′-bipyridyldiol.[72] It seems that FK(S_1) and FK(T_1) play predominant roles over BK(S_1) and BK(T_1) in the reverse ESIPT channel.

OHBA exhibits a rather fast internal conversion (IC) from the electronically excited state to the ground state.[17] It was noted that the time scale varied with the structure of the molecule by 3 orders of magnitude and between IC times of about 150 fs for 2-(2′-hydroxy-5′-methylphenyl) benzotriazole (TINUVINP)[73] to up to several hundred picoseconds for HBT.[74] The strong variation in the time scale for the IC process was supposedly due to the barrier that arises from an avoided crossing between the $\pi\pi^*$ and the $\pi\sigma^*$ states. Stock et al.[35] found a 55 ps time constant for the S_1 lifetime of FK(S_1) to convert to another species and observed an important out-of-plane vibrational mode in the lower-frequency region during this conversion process. They assigned this lower-frequency out-of-plane vibrational mode to a Fermi resonance but without taking into consideration the possible excited-state proton rotamerization of FK(S_1). The proton-transfer isomerization and various rotamerizations of OHBA in the ground and excited states were studied using CIS and MP2 levels with a 6-31+G* basis set.[30] The energies required to excite each of the conformers (E(S_0), FK(S_0), and various rotamers of E(S_0)) to the $^1n\pi^*$,$^3n\pi^*$,$^1\pi\pi^*$,and $^3\pi\pi^*$ excited states were reported. While this provides us detailed information about the competition between rotamerization and proton-transfer isomerization for OHBA, the energetics of the rotamers BK(S_1) and BK(T_1) in the ESIPT processes is still missing. Thus our present study helps to provide some supplementary information about the role of the proton rotamerization between FK(S_1) and BK(S_1) in the internal conversion process. The rotamerization between FK(S_1) and BK(S_1) is energetically accessible in the S_1 excited state because their energy difference is very small (2.5 kcal/mol) and the barrier is moderate (8.2 kcal/mol). If this rotamerization (one of the internal conversions) process occurs, then the rotamerization rate is expected to depend largely on the excitation energy due to the relatively higher barrier, and a lower-frequency out-of-plane vibrational mode is expected. This obviously is consistent with the transient absorption experiments that display a strong internal conversion rate dependence on the excitation energy and an important lower-frequency out-of-plane vibration mode.[35]

Conclusion

CT/PT band resonance Raman spectra were acquired for OHBA in cyclohexane solution. The resonance Raman spectra and intensity analysis of these spectra indicate that most of the short-time photodissociation dynamics in the Franck−Condon region occurs mainly along the nominal C=CH in-plane bend + C−O−H in-plane bend ν_{14} ($|\Delta| = 0.65$, $\lambda = 279$) and the nominal C=C−C(=O) in-plane bend + C=C−C(−OH) in-plane bend ν_{37} ($|\Delta| = 1.55$, $\lambda = 317$) mode, the nominal C=C−O(OH) in-plane bend + C=C−C(=O) in-plane bend ν_{33}

($|\Delta| = 0.78$, $\lambda = 138$), and the nominal ring deformation + C−C(H)═O in-plane ν_{30} ($|\Delta| = 0.63$, $\lambda = 133$), accompanied by moderate to smaller components along 10 other normal modes. These results for OHBA were compared to those previously reported for OHAP and reveal that among the 2808 cm^{-1} total vibrational reorganizational energy of OHAP more vibrational reorganizational energy is partitioned into the benzene-ring-related ring deformation or C═C−H in-plane bending modes, while among the 1506 cm^{-1} total vibrational reorganizational energy of OHBA more vibrational reorganizational energy is distributed along the ESIPT-relevant C−C═O/C−O−H bending modes. These distinct differences in the Franck−Condon region ESIPT dynamics between OHBA and OHAP are ascribed to the nature of the π^* orbital of OHAP that displays an excited-state supraconjugation interaction between the benzene ring group and the CH_2 group. We briefly discussed possible implications for this behavior for the photochemistry of OHBA.

Acknowledgment. This work was supported by grants from the National Science Foundation of China (Grant Nos. 20573097 and 20273062), Zhejiang National Science Foundation (Grant No. R405465), EYTP, MOE of China (Grant No. 1918) to X.Z. and from the Research Grants Council of Hong Kong (Grant No. HKU 7036/04P), the award of a Croucher Foundation Senior Research Fellowship (2006−2007) from the Croucher Foundation, and an Outstanding Researcher Award (2006) from the University of Hong Kong to D.L.P.

Supporting Information Available: Additional figures and table. This material is available free of charge via the Internet at http://pubs.acs.org.

References and Notes

(1) Weller, A. Z. *Electrochemistry* **1956**, *60*, 1144.
(2) Limbach, H. H.; Manz, J. *Ber. Bunsen−Ges. Phys. Chem.* **1998**, *102*, 289.
(3) (a) Hashimoto, S.; Sasaki, M.; Takeuchi, H.; Needleman, R.; Lanyi, J. K. *Biochemistry* **2002**, *41*, 6495. (b) Szundi, I.; Eps, N. V.; Einarsdóttir, Ó. *Biochemistry* **2003**, *42*, 5074.
(4) Chou, P. T. *J. Chin. Chem. Soc.* **2001**, *48*, 651.
(5) Chou, P. T.; McMorrow, D.; Aartsma, T. J.; Kasha, M. *J. Phys. Chem.* **1984**, *88*, 4596.
(6) Kasha, M. *Acta Physiol. Pol. A* **1987**, *71*, 717.
(7) Barbara, P. F.; Walsh, P. K.; Brus, L. E. *J. Phys. Chem.* **1989**, *93*, 29.
(8) Ferrer, M. L.; Acuña, A. U.; Amat-Guerri, F.; Costela, A.; Figuera, J. M.; Florido, F.; Sastre, R. *Appl. Opt.* **1994**, *33*, 2266.
(9) Douhal, A.; Sastre, R. *Chem. Phys. Lett.* **1994**, *219*, 91.
(10) Kuldová, K.; Corval, A.; Trommsdorff, H. P.; Lehn, J. M. *J. Phys. Chem. A* **1997**, *101*, 6850.
(11) Martinez, M. L.; Cooper, W. C.; Chou, P. T. *Chem. Phys. Lett.* **1992**, *193*, 151.
(12) Heller, H. J.; Blattmann, H. R. *Pure Appl. Chem.* **1973**, *36*, 141.
(13) Werner, T.; Woessner, G.; Kramer, H. E. A. In *Photodegradation and Photostabilization of Coatings*; Pappas, S. P., Winslow, F. H., Eds.; ACS Symposium Series 151; American Chemical Society: Washington, DC, 1981; p 1.
(14) Lukeman, M.; Wan, P. *Chem. Commun.* **2001**, 1004.
(15) Lukeman, M.; Wan, P. *J. Am. Chem. Soc.* **2002**, *124*, 9548.
(16) Flegel, M.; Lukeman, M;, Huck, L.; Wan, P. *J. Am. Chem. Soc.* **2004**, *126*, 7890.
(17) Arthen-Engeland, T.; Bultmann, T.; Ernsting, N. P.; Rodriguez, M. A.; Thiel, W. *Chem. Phys.* **1992**, *163*, 43.
(18) Lochbrunner, S.; Schultz, T.; Schmitt, M.; Shaffer, J. P.; Zgierski, M. Z.; Stolow, A. *J. Chem. Phys.* **2001**, *114*, 2519.
(19) Herek, J. L.; Pederson, S.; Benares, L.; Zewail, A. H. *J. Chem. Phys.* **1992**, *97*, 9046.
(20) Ameer-Beg, S.; Ormson, S. M.; Brown, R. G.; Matousek, P.; Towrie, M.; Nibbering, E. T. J.; Foggi, P.; Neuwahl, F. V. R. *J. Phys. Chem. A* **2001**, *105*, 3709.
(21) Lärmer, F.; Elsaesser, T.; Kaiser, W. *Chem. Phys. Lett.* **1988**, *148*, 119.
(22) Chudoba, C.; Riedle, E.; Pfeiffer, M.; Elsaesser, T. *Chem. Phys. Lett.* **1996**, *263*, 622.
(23) Lochbrunner, S.; Wurzer, A. J.; Riedle, E. *J. Phys. Chem. A* **2003**, *107*, 10580.
(24) Neuwahl, F. V. R.; Foggi, P.; Brown, R. G. *Chem. Phys. Lett.* **2000**, *319*, 157.
(25) Ernsting, N. P.; Kovalenko, S. A.; Senyushkina, T.; Saam, J.; Farztdinov, V. *J. Phys. Chem. A* **2001**, *105*, 3443.
(26) Nagaoka, S.; Nagashima, U. *Chem. Phys.* **1989**, *136*, 153.
(27) Dick, B. *J. Phys. Chem.* **1990**, *94*, 5752.
(28) Gordon, M. S. *J. Phys. Chem.* **1996**, *100*, 3974.
(29) Sobolewski, A. L.; Domcke, W. *Chem. Phys.* **1998**, *232*, 257.
(30) Čuma, M.; Scheiner, S.; Kar, T. *J. Am. Chem. Soc.* **1998**, *120*, 10497.
(31) Čuma, M.; Thompson, C.; Scheiner, S. *J. Comput. Chem.* **1998**, *19*, 129.
(32) Scheiner, S. *J. Phys. Chem. A* **2000**, *104*, 5898.
(33) Mitra, S.; Mukherjee, S. *J. Lumin.* **2006**, *118*, 1.
(34) Cho, D. W.; Kim, S. H.; Yoon, M.; Jeoung, S. C. *Chem. Phys. Lett.* **2004**, *391*, 314.
(35) Stock, K.; Bizjak, T.; Lochbrunner, S. *Chem. Phys. Lett.* **2002**, *354*, 409.
(36) Peteanu, L. A.; Mathies, R. A. *J. Phys. Chem.* **1992**, *96*, 6910.
(37) Wang, Y.-Q.; Wang, H.-G.; Zhang, S.-Q.; Pei, K.-M.; Zheng, X.; Phillips, D. L. *J. Chem. Phys.* **2006**, *125*, 214506.
(38) Billinghurst, B. E.; Loppnow, G. R. *J. Phys. Chem. A* **2006**, *110*, 2353.
(39) Billinghurst, B. E.; Yeung, R.; Loppnow, G. R. *J. Phys. Chem. A* **2006**, *110*, 6185.
(40) Neugebauer, J.; Hess, B. A. *J. Chem. Phys.* **2004**, *120*, 11564.
(41) Sobolewski, A. L.; Domcke, W. *Chem. Phys.* **1994**, *184*, 115.
(42) Sobolewski, A. L.; Domcke, W. *Phys. Chem. Chem. Phys.* **1999**, *1*, 3065.
(43) Kwok, W. M.; Phillips, D. L. *Chem. Phys. Lett.* **1995**, *235*, 260.
(44) Kwok, W. M.; Phillips, D. L. *J. Chem. Phys.* **1996**, *104*, 2529.
(45) Phillips, D. L.; Myers, A. B. *J. Raman Spectrosc.* **1997**, *28*, 839.
(46) Zheng, X.; Phillips, D. L. *J. Chem. Phys.* **1998**, *108*, 5772.
(47) Zheng, X.; Lee, C. W.; Phillips, D. L. *J. Chem. Phys.* **1999**, *111*, 11034.
(48) Zheng, X.; Li, Y. L.; Phillips, D. L. *J. Phys. Chem. A* **2004**, *108*, 8032.
(49) Zhu, X. M.; Zhang, S. Q.; Zheng, X.; Phillips, D. L. *J. Phys. Chem. A* **2005**, *109*, 3086.
(50) Weng, K. F.; Shi, Y.; Zheng, X.; Phillips, D. L. *J. Phys. Chem. A* **2006**, *110*, 851.
(51) Lee, S. Y.; Heller, E. J. *J. Chem. Phys.* **1979**, *71*, 4777.
(52) Heller, E. J.; Sundberg, R. L.; Tannor, D. J. *J. Phys. Chem.* **1982**, *86*, 1822.
(53) Myers, A. B.; Mathies, R. A. In *Biological Applications of Raman Spectroscopy*; Spiro, T. G., Ed.; Wiley: New York, 1987; Vol. 2, p 1.
(54) Myers, A. B. In *Laser Techniques in Chemistry*; Myers, A. B., Rizzo, T. R., Eds.; Wiley: New York, 1995; p 325.
(55) Becke, A. *J. Chem. Phys.* **1986**, *84*, 4524.
(56) Lee, C.; Yang, W.; Parr, R. G. *Phys. Rev. B* **1988**, *37*, 785.
(57) Hegarty, D.; Robb, M. A. *Mol. Phys.* **1979**, *38*, 1795.
(58) Frisch, M. J.; Trucks, G. W.; Schlegel, H. B.; Scuseria, G. E.; Robb, M. A.; Cheeseman, J. R.; Zakrzewski, V. G.; Montgomery, J. A., Jr., Stratmann, R. E.; Burant, J. C.; Dapprich, S.; Millam, J. M.; Daniels, A. D.; Kudin, K. N.; Strain, M. C.; Farkas, O.; Tomasi, J.; Barone, V.; Cossi, M.; Cammi, R.; Mennucci, B.; Pomelli, C.; Adamo, C.; Clifford, S.; Ochterski, J.; Petersson, G. A.; Ayala, P. Y.; Cui, Q.; Morokuma, K.; Malick, D. K.; Rabuck, A. D.; Raghavachari, K.; Foresman, J. B.; Cioslowski, J.; Ortiz, J. V.; Baboul, A. G.; Stefanov, B. B.; Liu, G.; Liashenko, A.; Piskorz, P.; Komaromi, I.; Gomperts, R.; Martin, R. L.; Fox, D. J.; Keith, T.; Al-Laham, M. A.; Peng, C. Y.; Nanayakkara, A.; Gonzalez, C.; Challacombe, M.; Gill, P. M. W.; Johnson, B.; Chen, W.; Wong, M. W.; Andres, J. L.; Gonzalez, C.; Head-Gordon, M.; Replogle, E. S.; Pople, J. A. *Gaussian 03*, revision B.02; Gaussian, Inc.: Wallingford, CT, 2003.
(59) Borisenko, K. B.; Hargittai, I. *J. Phys. Chem.* **1993**, *97*, 4080.
(60) Frisch, M. J.; Scheiner, A. C.; Schaefer, H. F., III.; Binkley, J. S. *J. Chem. Phys.* **1985**, *82*, 4194.
(61) Gilli, G.; Bellucci, F.; Ferretti, V.; Bertolasi, V. *J. Am. Chem. Soc.* **1989**, *111*, 1023.
(62) Martin, J. M. L.; Alsenoy, C. V. *J. Phys. Chem.* **1996**, *100*, 6973.
(63) Sim, F.; St-Amant, A.; Papai, I.; Salahub, D. *J. Am. Chem. Soc.* **1992**, *114*, 4391.
(64) Lampert, H.; Mikenda, W.; Karpfen, A. *J. Phys. Chem.* **1996**, *100*, 7418.
(65) Lampert, H.; Mikenda, W.; Karpfen, A. *J. Phys. Chem. A* **1997**, *101*, 2254.
(66) Trulson, M. O.; Mathies, R. A. *J. Chem. Phys.* **1986**, *84*, 2068.

(67) Nishiya, T.; Yamauchi, S.; Hirota, N.; Baba, M.; Hanazaki, I. *J. Phys. Chem.* **1986**, *90*, 5730.
(68) Chou, P. T.; Chiou, S. C.; Yu, W. S.; Wu, G. R.; Wei, T. H. *Chem. Phys. Lett.* **2003**, *370*, 747−755.
(69) Prieto, M. F. R.; Nickel, B.; Grellmann, K. H.; Mordzinski, A. *Chem. Phys. Lett.* **1988**, *146*, 387.
(70) Grellmann, K. H.; Mordzinski, A.; Heinrich, A. *Chem. Phys.* **1989**, *136*, 201.
(71) Chou, P. T.; Studer, S. L.; Martinez, M. L. *Chem. Phys. Lett.* **1991**, *178*, 393.
(72) Grabowska, A.; Borowicz, P.; Martire, D. O.; Braslavsky, S. E. *Chem. Phys. Lett.* **1991**, *185*, 206.
(73) Chudoba, C.; Lutgen, S.; Jentzsch, T.; Riedle, E.; Woerner, M.; Elsaesser, T. *Chem. Phys. Lett.* **1995**, *240*, 35.
(74) Barbara, P. F.; Brus, L. E.; Rentzepis, P. M. *J. Am. Chem. Soc.* **1980**, *102*, 5631.